minerals

MDPI

Article

Effect of High-P Iron Ores on the Phases Developed During Sintering

Isis R. Ignacio [1], Natalie A. Ware [1], Mark I. Pownceby [2,*], Nathan A. S. Webster [2] and Aaron Torpy [2]

[1] CSIRO Mineral Resources, 1 Technology Ct, Pullenvale, QLD 4069, Australia; isisignacio@gmail.com (I.R.I.); natalie.ware@csiro.au (N.A.W.)
[2] CSIRO Mineral Resources, Research Way, Clayton, VIC 3168, Australia; nathan.webster@csiro.au (N.A.S.W.); aaron.torpy@csiro.au (A.T.)
* Correspondence: mark.pownceby@csiro.au

Abstract

This study investigates the effects of phosphorus (P) on the phases developed during sintering and their impact on the stability of key phases in iron ore sinter, particularly the silico-ferrite of calcium and aluminum ('SFCA') series of phases. Two complementary systems were studied: an industrially representative blend of natural iron ores (JSM) and a synthetic high-purity SFCA analogue (SA) system designed to promote controlled SFCA formation. Phosphorus was added as hydroxyapatite (HA) at levels of 0.5, 1.0, 1.5 and 5 wt.%. To simulate a standard sintering profile, experiments were conducted over a range of temperatures for 3 min in a controlled low-oxygen-potential atmosphere of $pO_2 = 5 \times 10^{-3}$ atm. A modified Bond Abrasion test was used to evaluate the tumble index (TI) strength of the samples, and the chemistry, mineralogy and microstructure of all sintered products were analyzed. Results indicated that all P-doped JSM samples fired within the temperature range of 1300 to 1330 °C met the minimum strength requirement (TI = 80%) for producing high-quality sinters. Adding small to medium amounts of HA ($\leq$1.5 wt.%) to both compositions had a limited impact on the overall mineral phases. Conversely, adding a high amount of HA (5 wt.%) encouraged the creation of Ca–Si–P phases. Analysis of the microstructure, minerals, and microchemistry indicated that P tended to segregate phases rich in phosphorus by interacting with calcium oxide and silica. The findings from the study highlight that at the low levels of P typically found in iron ores, there is no significant impact on the strength, mineralogy and phases formed during sintering.

Keywords: iron ore sintering; phosphorus; silico-ferrite of calcium and aluminum; hydroxyapatite; mineralogy; microstructure; tumble index

Check for updates

Academic Editor: Zhiyong Gao

Received: 17 June 2026
Revised: 15 July 2026
Accepted: 22 July 2026
Published: 24 July 2026

Copyright: © 2026 by the authors. Licensee MDPI, Basel, Switzerland. This article is an open access article distributed under the terms and conditions of the Creative Commons Attribution (CC BY) license.

1. Introduction

Iron ore sintering is an essential agglomeration process in the ironmaking industry, where fine iron ore, fluxes, and fuel are thermally processed to produce sinter, a porous, solid product used as feed in the blast furnace. The quality of sinter depends significantly on the types and proportions of mineral phases developed during sintering. Among these, silico-ferrites of calcium and aluminum (SFCA, SFCA-I and SFCA-III) are key bonding phases that contribute to the mechanical strength and reducibility of the sinter [1]. Understanding the conditions that promote or hinder the formation and stability of these phases is critical for optimizing sinter performance.

Phosphorus is a common impurity in iron ores, often present in gangue minerals such as apatite or associated with iron oxides [2]. When present with iron oxides, phosphorus has been shown to be mainly associated with the iron oxyhydroxide phase, goethite (FeO.OH), along with other impurities such as silica (Si) and alumina (Al) [3]. Studies by Dukino et al. [4] and Pownceby et al. [3] revealed that P levels depend not only on the amount of goethite but also on its microtextural type, with late-formed colloform goethite, found in cracks and pore networks, as well as vitreous goethite consistently showing the highest P levels.

High-P ores have traditionally been avoided due to their detrimental effects on the mechanical properties of steel [5] and the costs associated with removing P during steelmaking. The removal of P from the initial iron ore feed materials through physical beneficiation techniques remains challenging, as these processes often lead to iron losses or result in residual P that persists through subsequent processing stages, ultimately appearing in sinter, pig iron, and steel. In contrast, chemical leaching methods can achieve higher P removal efficiencies; however, they are typically more complex, more costly, and frequently necessitate thermal pre-treatment to enhance effectiveness [6]. As a result, increasing demand for iron ore, coupled with the depletion of high-grade low-P reserves, has renewed interest in evaluating the suitability of high-P ores in sinter blends [7].

While the steelmaking consequences of P are well known, its influence on sintering reactions and mineral phases formation remains less understood. For example, it is known that P reduces the mechanical properties of Fe alloys by acting as a surface-active element in melts [8]. This means that P does not stay evenly mixed in the liquid, but rather it migrates to the surface, lowering the surface tension. However, sinter is never completely molten; rather, it is a solid product formed when partially molten particles become bonded together while the bulk remains solid. This makes the influence of P more complex to predict.

Previous studies, such as that of Patrick & Lovel [9], showed that P tends to partition preferentially into dicalcium silicate (C_2S), potentially altering the phase assemblage and affecting the formation or stability of key bonding phases like the SFCA series of phases. These interactions could have significant implications for sinter quality, but further investigation is required to confirm this behavior and evaluate its practical impacts.

The present work investigates, at the laboratory scale, the influence of P on phase formation during sintering and the consequent effects on phase stability and sinter quality under two complementary conditions: (i) a blend of natural iron ores previously optimized for sintering studies, representative of typical industrial practice, and (ii) a synthetic system formulated from high-purity analytical reagents to promote the formation of pure SFCA phases and enable controlled assessment of phase stability. Phosphorus was introduced in varying concentrations to both systems. Although the target P content in iron ores for steelmaking is generally below 0.1 wt.%, with many producers and standards imposing even stricter limits ($\leq$0.08 wt.%) [10–12], this study employs higher concentrations to accentuate the effects of P on sintering behavior.

Samples were sintered over a range of temperatures using the CSIRO-developed, laboratory-scale sintering method [13] designed to simulate the sintering conditions in industrial sinter. The products were characterized using a suite of analytical techniques including X-ray fluorescence spectroscopy (XRF), quantitative X-ray diffraction (QXRD), in situ X-ray diffraction, reflected light optical microscopy, scanning electron microscopy (SEM) and electron probe microanalysis (EPMA). Sinter strength was further evaluated using a modified laboratory scale tumble index (TI) test to establish correlations between mineralogical evolution and mechanical performance. By systematically examining both natural and synthetic systems, this study offers insights into the mechanisms by which P influences sinter mineralogy and phase stability.

2. Materials and Methods

2.1. Sample Preparation

2.1.1. Ore Blend Samples (JSM)

The ore blend used in this experiment is based on the typical Japanese Steel Mill (JSM) sinter blend used in previous works [14,15], which consists of a blend of −1 mm natural ore from different sources, and ultrafine fluxes. The JSM ore blend presents favorable chemical, physical and mineralogical characteristics, performing well in sintering studies [14]. Table 1 shows the composition of the JSM blend, which presents low levels of P (0.04 wt.%). Basicity is the CaO/SiO_2 ratio, and $LOI_{900°C}$ is the loss on ignition after heating to 900 °C.

Table 1. Composition of the simulated JSM base blend (wt.%).

	Fe_2O_3	Fe	CaO	SiO_2	Al_2O_3	Mn	MgO	P	Basicity	$LOI_{900°C}$
JSM	71.71	50.15	9.68	4.42	1.61	0.24	0.13	0.04	2.20	11.99

Since apatite is the most frequently encountered P-rich phase in iron ores [2], the P source used in the experiments was analytical-grade hydroxyapatite (HA) ($Ca_5(PO_4)_3OH$, 99%, Sigma-Aldrich, St Louis, MO, USA), in powder form. For the experiments, HA was incorporated into the standard JSM blend at varying levels (0.5, 1.0, 1.5 and 5 wt.%). The lower additions (0.5–1.5 wt.% HA) bracket the range of P contents relevant to high-P iron ores and concentrates, while the highest addition (5 wt.% HA, equivalent to ~1 wt.% P) exceeds typical ore-derived P levels and was included as a deliberately extreme, mechanism-revealing composition to accentuate and clarify the effects of P on phase formation rather than to represent an industrially realistic blend. Table 2 shows the composition of the samples after P addition.

Table 2. Composition after mixing HA with the JSM base blend (wt.%).

Samples	Fe_2O_3	CaO	SiO_2	Al_2O_3	P	Basicity
JSM Base	71.71	9.68	4.40	1.66	0.04	2.20
JSM + 0.5% HA	71.35	9.79	4.38	1.65	0.14	2.24
JSM + 1% HA	70.99	9.91	4.36	1.64	0.23	2.27
JSM + 1.5% HA	70.63	10.02	4.35	1.63	0.33	2.31
JSM + 5% HA	68.87	10.76	4.28	1.59	1.06	2.51

Optimal basicity in iron ore sinters generally ranges between 1.6 and 2.8 [16]. The addition of HA to the sinter mix can influence the overall basicity, as it introduces both CaO (a basic oxide) and P_2O_5, which, although not directly considered in basicity calculations, significantly affect phase formation. Since the CaO content increases while SiO_2 remains constant, the basicity of the mixture consequently rises with increasing phosphorus. At elevated temperatures (800–1200 °C), P_2O_5 readily reacts with other oxides to form phosphate-based compounds such as calcium phosphates (e.g., $Ca_3(PO_4)_2$ and $Ca_2Fe_2O_5$–P_2O_5 solid solutions). These reactions can modify the formation and stability of SFCA phases, thereby influencing the overall sinter mineralogy. In this study, the addition of HA resulted in only a modest increase in basicity, with the highest value (B = 2.51) observed at 5 wt.% HA, corresponding to a 14% rise in basicity relative to the base mix. As HA addition necessarily introduces both P and additional CaO, the effects of P and basicity on phase formation and sinter strength discussed in the following sections cannot be fully separated experimentally; however, given that the associated basicity increase is modest even at the highest HA addition, the phase and strength trends reported are interpreted primarily as reflecting the effect of P.

2.1.2. Synthetic SFCA Samples (SA)

Synthetic systems are commonly used to study mineralogical trends in sintering, as they behave similarly to natural iron fine sinters when varying the composition [17]. In this series of experiments, we aimed to systematically examine the effect of P on the formation and stability of the key SFCA series of bonding phases typically present in iron ore sinter. A second set of samples was therefore produced by mixing fine-grained synthetic hematite (Fe_2O_3, ≥99%, Sigma-Aldrich, St Louis, MO, USA), calcite ($CaCO_3$, 99.0%, Sigma-Aldrich, St Louis, MO, USA), quartz (SiO_2, 99.9%, LABCHEM, APS Finechem, NSW, Australia), and gibbsite ($Al(OH)_3$, 99.9%, UNILAB, APS Finechem, NSW, Australia) forming the sinter analogue (SA) base composition. The SA composition is a high-purity synthetic analogue designed to promote controlled SFCA formation and is not intended to reproduce bulk industrial sinter chemistry. The nominal mixing ratio of each reagent (Table 3) was based on previous work by [18]. This mixture was equivalent to mixture SM4/5, which was shown by Scarlett et al. [19] to produce single-phase SFCA under equilibrium conditions at high temperature and in air, and it has subsequently been utilized in numerous in situ XRD investigations into sinter phase formation mechanisms (e.g., Webster et al. [20]).

Table 3. Nominal mixing ratio of the reagents used for SA samples (wt.%).

Samples	Fe_2O_3	$CaCO_3$	SiO_2	$Al(OH)_3$	HA
SA base	68.04	22.10	3.13	6.73	0.00
SA base + 0.5% HA	67.70	21.99	3.11	6.70	0.50
SA base + 1.0% HA	67.37	21.88	3.10	6.66	0.99
SA base + 1.5% HA	67.03	21.77	3.08	6.63	1.48
SA base + 5% HA	64.80	21.05	2.98	6.41	4.76

Analytical grade HA was added at varied amounts (0.5, 1, 1.5 and 5 wt.%) into the SA base mix. The powders were uniformly mixed using a ball mill to ensure homogeneity. Table 4 shows the new chemical composition of the SA samples.

Table 4. Final composition of the sinter analogue (SA) samples with HA addition (wt.%).

Sample	Fe_2O_3	CaO	SiO_2	Al_2O_3	P	Basicity
SA base	77.35	14.07	3.56	5.00	0.00	3.95
SA base + 0.5% HA	77.16	14.19	3.55	4.99	0.10	4.00
SA base + 1.0% HA	76.98	14.31	3.54	4.97	0.18	4.04
SA base + 1.5% HA	76.79	14.43	3.53	4.95	0.28	4.09
SA base + 5% HA	75.28	15.14	3.49	4.84	0.93	4.34

2.2. Compact Sintering Method and TI Test

Laboratory-based compact sinter tests were conducted using the method described in Clout and Manuel [13]. Four-gram pellet samples (~12 mm diam. and 12 mm in height) were compressed to 10,000 kPa pressure using a hydraulic press and fired in a horizontal tube furnace using the same standard heating profile from previous works [13,15]. Samples were fired in pairs at different maximum temperatures (T_{max}) of 1250, 1300 and 1330 °C for 3 min in a controlled low-oxygen-potential atmosphere of $pO_2 = 5 \times 10^{-3}$ atm, obtained with a pre-mixed 99.5% N_2/0.5% O_2 gas mixture. This short holding time reflects the typical residence time at peak temperature in industrial sintering, and phase assemblages obtained under these conditions are known to be kinetically controlled rather than equilibrium products; longer holding times (e.g., ~120 min) more closely approach equilibrium and can produce markedly different phase assemblages [21]. This pO_2 level is commonly selected

in laboratory studies as it was found to maximize the formation of calcium ferrites whilst still producing mineral assemblages like those found in industrial iron ore sinters [22].

The modified Bond Abrasion test was used to evaluate the TI strength of the samples. In this method, the fired samples are placed in pairs in a rotating steel drum fitted with internal lifters. Each pair of pellets was tumbled together to yield a single TI value per composition and temperature rather than independent replicate measurements. The drum is rotated at a fixed speed for a defined number of revolutions, subjecting the material to continuous impact and abrasion. After tumbling, the material was sieved, and the relative compact TI is given as the percentage of the material retained at above 2 mm. A TI of 80% is considered equivalent to a TI of 65% in a standard pot-grate sinter test [13]. A TI value of 65% in the pot-grate sinter test is considered the minimum strength required for acceptable iron ore sinter. This test has previously been used in compact sinter studies [15,23,24] to provide strength versus temperature melting curves for sinter analogue samples fired at a range of temperatures.

2.3. Characterization Techniques

Material recovered after the TI testing was used for further characterization studies. Larger pieces of the pellets were set in epoxy resin using 2.5 cm round molds and allowed to cure before sectioning to reveal a fresh surface. The sectioned surface of each block was then polished to optical flatness using fine-grit sandpapers before final polishing was conducted using successively finer 6, 3 and 1 µm diamond pastes. All samples were polished using water-free polishing liquids to avoid dissolving crucial phases (e.g., larnite) during preparation. The polished blocks were used in subsequent optical microscopy, SEM and EPMA examinations. The remaining materials from the TI tests were micronized using a mechanical grinding mill and used for QXRD and XRF analysis.

Optical, reflected light microscopy was carried out by placing the polished samples on a moving stepping stage fixed to a ZEISS Axioplan2 microscope (ZEISS, Oberkochen, Germany). Images of the microstructures were captured with AxioVision 4.7 software (Carl Zeiss). This technique enables a qualitative analysis of the main textural features developed during sintering. For example, optical examination allows for the clear differentiation of iron oxides like hematite and magnetite as well as distinguishing between primary and secondary hematite sub-types and various SFCA morphologies [25].

Scanning electron microscopy combined with energy dispersive X-ray spectrometry (SEM-EDS) was carried out on selected samples for microstructure evaluation and microanalytical study to observe the P distribution. All polished blocks were carbon coated with a thin 10 nm layer of carbon prior to analysis to prevent charge build-up on the surface. SEM analyses were carried out using a ZEISS Gemini, series Sigma 300VP (ZEISS, Oberkochen, Germany), at a high vacuum, a working distance of 13 mm, and a high voltage of 15 kV. Standardless EDS analyses were carried out using the Esprit 2.3 software by Bruker.

Selected samples were also examined using high-resolution EPMA. EPMA mapping data from randomly selected areas covering 1400 × 1400 µm on each sample was obtained using a JEOL field emission gun electron probe micro-analyzer (Model JXA-8530F FEG-EPMA, JEOL, Tokyo, Japan) equipped with four wavelength dispersive (WD) spectrometers and two Bruker XFLASH energy dispersive (ED) spectrometers (Bruker, Billerica, MA, USA). The elements mapped using the WD spectrometers were Al, P, Fe and Ca. Standards used to calibrate the EPMA WD spectrometers prior to mapping were synthetic aluminum phosphate ($AlPO_4$), wollastonite ($CaSiO_3$) and hematite (Fe_2O_3). Elements that were not measured by WD spectroscopy were measured using two ED spectrometers operating in parallel. Measuring both ED and WD signals simultaneously ensured that the complete chemical spectrum, at each step interval in the map, was obtained. The microprobe was

operated at an accelerating voltage of 15 kV, a beam current of 50 nA, a step size of 1 µm (in x and y), and a counting time of 30 ms per step during mapping. Data analysis included hyperspectral clustering using the software package Chimage v.10.0.34 [26,27] including quantitative determination of cluster compositions following methods described in Torpy et al. [28]. Due to fine-grained intergrowths in this specimen, the phase maps were produced using n-dimensional linear least squares deconvolution to resolve sub-pixel compositional mixtures (ibid.). The composition of phases was calculated by standards-based quantitative analysis of the ED spectra using the in-house EQuiP v1.24.08 software, which employs the exponential Pouchou and Pichoir (XPP) matrix correction algorithm [29] as implemented in the STRATAgem software module (remX GmbH, Bruchsal, Germany).

XRF analysis was carried out by fusing approximately 0.5 g of sample with 5 g of 12:22 lithium borate flux in a Pt/Au (95%/5%) crucible, with weights recorded to ±0.1 mg. The mixture was melted in an automated XRF Scientific VFD Phoenix fusion machine (XRF Scientific, Osborne Park, WA, Australia) at ~1000 °C for 3 min, homogenized by swirling, and cast into a pre-heated 30 mm Pt/Au (95%/5%) mold to form a stable lithium borate glass disk. Disks were analyzed on a Bruker S8 Tiger 4 kW WD-XRF (Bruker, Billerica, MA, USA) with a Rh X-ray tube, using optimized peak/background conditions for each element. Elemental concentrations were derived from CSIRO-developed calibrations using high-purity standards, with matrix effects corrected via Bruker's variable concentration 'Alphas' method. Results are reported as wt.% oxides to three significant figures, with uncertainty reflected in the final digit.

QXRD analysis was carried out on micronized powder samples. XRD patterns were collected in Bragg–Brentano geometry on a Panalytical Empyrean diffractometer equipped with a Co tube operated at 40 kV and 40 mA (Malvern Panalytical B.V., Almelo, The Netherlands). On the incident beam side, a programmable divergent slit and beam mask in the iCore optics defined the X-ray illumination on the sample. Patterns were collected from 4 to 80° in steps of 0.017° 2θ with a counting time of 0.5 s per step, for an overall counting time of approximately 35 min, using a fast 1Der detector operated in 1D mode with an active length of 2.1223°. Phase identification was performed on individual datasets using Panalytical HighScore Plus V5.2 (Malvern Panalytical B.V., Almelo, The Netherlands, 2023) incorporating the International Centre for Diffraction Data (ICDD) PDF-5+ 2025 database (ICDD, Newtown Square, USA, 2025). Quantitative phase analysis was conducted using the Rietveld method as implemented in Topas V7 (Bruker, Karlsruhe, Germany, 2022).

In situ XRD experimentation was conducted with a selected green sample blend (before compacting and sintering) using a PANalytical Empyrean diffractometer fitted with an Anton Paar 16N high-temperature chamber incorporating a Pt heating strip with an 8 × 20 × 0.2 mm sample well. XRD data were collected in Bragg–Brentano diffraction geometry using an iCore incident beam optic incorporating a programmable divergence slit and incident beam mask for a constant X-ray beam illumination on the sample of 4 × 7 mm. The 1Der detector was operated in 1D mode with an active length of 2.1223°, and the step size of data acquisition was 0.033° 2θ. The X-ray wavelength was 1.789 Å (0.1789 nm) from a Co X-ray tube. The samples were heated at $pO_2 = 5 \times 10^{-3}$ atm at a rate of 20 °C min^{-1} for 25–600 °C, then 10 °C min^{-1} for 600–1350 °C; they were then cooled at a rate of 2 °C min^{-1} for 1350–1000 °C and 50 °C min^{-1} for 1000–25 °C, matching previous work [30]. Data was collected continuously during heating and cooling, with individual datasets collected for 2 min over the range 5° < 2θ < 50°. The Anton Paar chamber was fed by a continuous flow of a 0.5% O_2 in N_2 gas mixture ($pO_2 = 5 \times 10^{-3}$ atm) during both heating and cooling. The decomposition of precursor phases and the formation of new phases were visualized as a contour plot of the diffracted peak intensity versus 2θ angle and temperature.

3. Results and Discussion

3.1. Relationship Between Temperature, P Concentration and Strength

Compacts made from the JSM blend were found to rapidly increase TI strength from 1250 to 1300 °C, reaching maximum strength at 1300 °C (Figure 1). At the lowest temperature of 1250 °C, when adding P from 0 to 1.5 wt.% HA, the maximum strength was observed in the sample prepared with 1% HA, although differences between all four samples were not significant. Similarly, for intermediate temperatures (1300 °C), there was no significant difference in strength observed for the samples with 0%–1.5% HA. At the highest temperature of 1330 °C, the samples with 1.0 and 1.5 wt.% HA appeared to slightly degrade in strength, although the difference was minimal. The sample with the highest phosphorus concentration (5 wt.% HA) behaved differently from all the others, initially exhibiting the lowest strength at the lower and intermediate temperatures (1250 and 1300 °C) but favoring higher strength at the highest temperature (1330 °C) examined. In summary, for the JSM samples, the blends maintained their strength, or slightly decreased, as the temperature increased to 1330 °C, except for the highest P sample (5 wt.% HA), which showed a slightly improved TI at 1330 °C. The general increase in TI with temperature for the JSM blend was expected and aligns with previous studies [13]. All the P-doped JSM samples fired between 1300 and 1330 °C achieved the minimum strength threshold (TI = 80%) required for high-quality sinters [17].

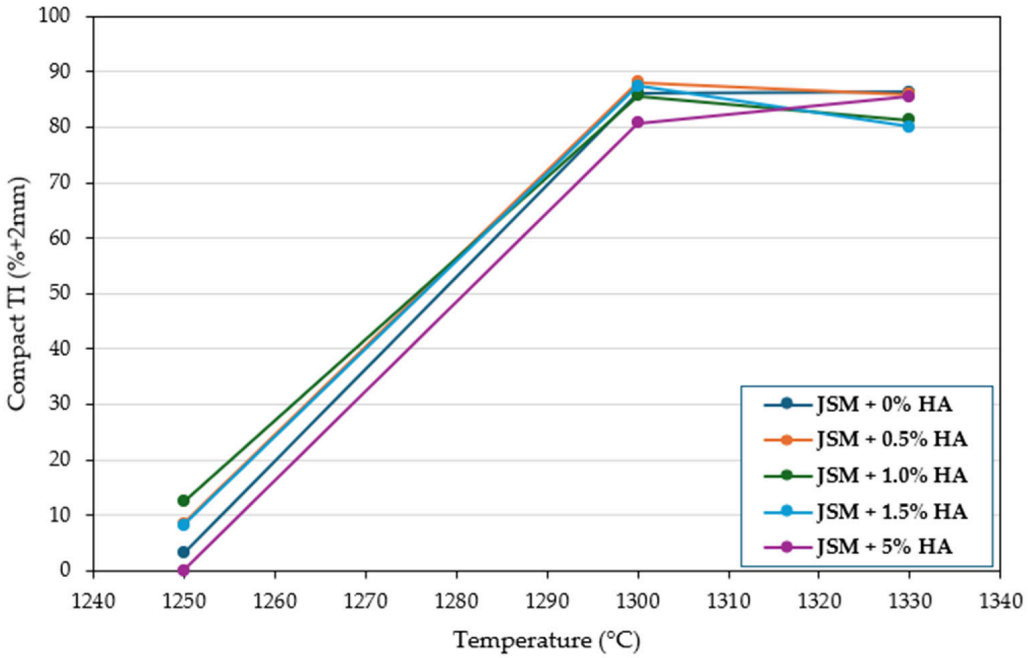


Figure 1. Compact tumble index (TI) versus temperature plot for the JSM blend samples at varying HA amounts (wt.%).

For the SA blend, samples were also found to exhibit an increase in TI strength from 1250 to 1300 °C (Figure 2). The major difference between the SA and JSM blend samples was that the SA samples achieved significantly higher strength at 1250 °C. However, like the JSM samples, the SA samples reached their maximum strength at 1300 °C and then slightly declined in strength at temperatures above 1300 °C. The more significant decline was observed for the high-P composition (5 wt.% HA), indicating that high-P content degrades strength at high temperatures.

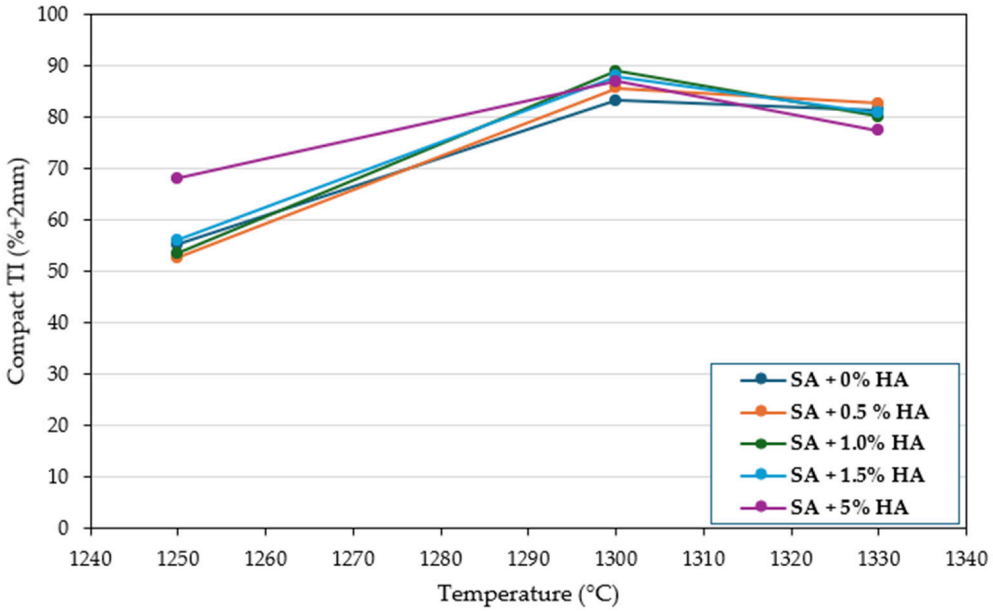


Figure 2. Compact tumble index (TI) versus temperature plot for the SA blend samples at varying HA amounts (wt.%).

The higher TI values at 1250 °C for the SA blend compared to the JSM blend are not unexpected, as the SA blend is designed to maximize the formation of high-strength SFCA bonding phases, which for the SA blend is achieved at ~1259 °C in the P-free system [12]. The larger improvement in strength for the 5 wt.% HA addition is, however, unusual, possibly suggesting some sort of stabilizing effect on SFCA formation at high P levels. An alternative explanation could be the formation of an additional high-strength, P-bearing phase that forms at intermediate temperatures; this is discussed further below.

The trends beyond 1250 °C are similar for both the JSM and SA blends. According to the in situ XRD data of Webster et al. [20], for the SA blend, melting of SFCA phases occurs beyond 1259 °C, leading to the formation of magnetite and melt. While the melting point of SFCA phases will change with composition, the difference is not expected to be very large, and we therefore expect that at 1300 °C the phase assemblage for the two blends would be similar (but differ slightly in proportions). As a result, there is no significant difference in strength observed between the blends at this point.

3.2. Sinter Mineralogy and Microstructures

3.2.1. Quantitative Phase Analysis

The evolutions of the major crystalline phases (hematite, SFCA, SFCA-I, SFCA-III and magnetite) with increasing P content at different temperatures (1250 °C, 1300 °C, and 1330 °C) are shown in Figures 3 and 4 for the JSM blend and SA samples, respectively, and in Figure 5 for both the JSM and SA samples. In contrast to the data shown in Figures 3 and 4, the P content in Figure 5 is shown as wt.% P obtained by XRF analysis of the final reacted pellets.

JSM Blend

The quantitative phase analysis of the JSM blend sinter samples determined by Rietveld refinement of the XRD data for experiments at 1250 °C, 1300 °C, and 1330 °C with varying HA additions (0–5 wt.%) is shown in Figure 3. Across all temperatures, the main crystalline phases identified were hematite, magnetite, 'SFCA'-type phases (SFCA, SFCA-I, and SFCA-III), and larnite (Ca_2SiO_4). Dicalcium-ferrite ($Ca_2Fe_2O_5$) and silico-phosphate ($Ca_5(SiO_4)(PO_4)_2$) phases were also present, but at lower amounts.

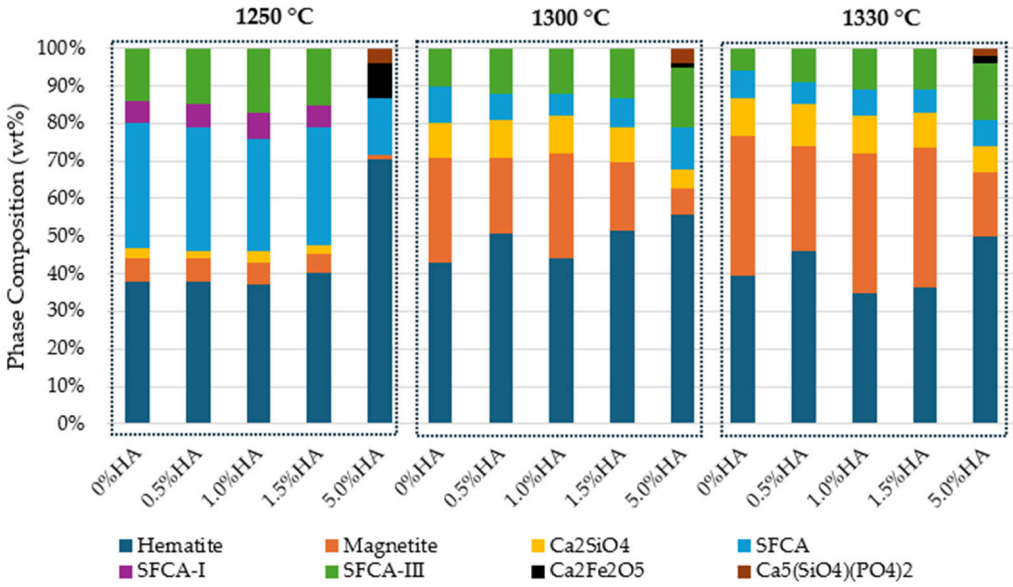


Figure 3. Results of Rietveld-based QXRD analysis of JSM blend samples.

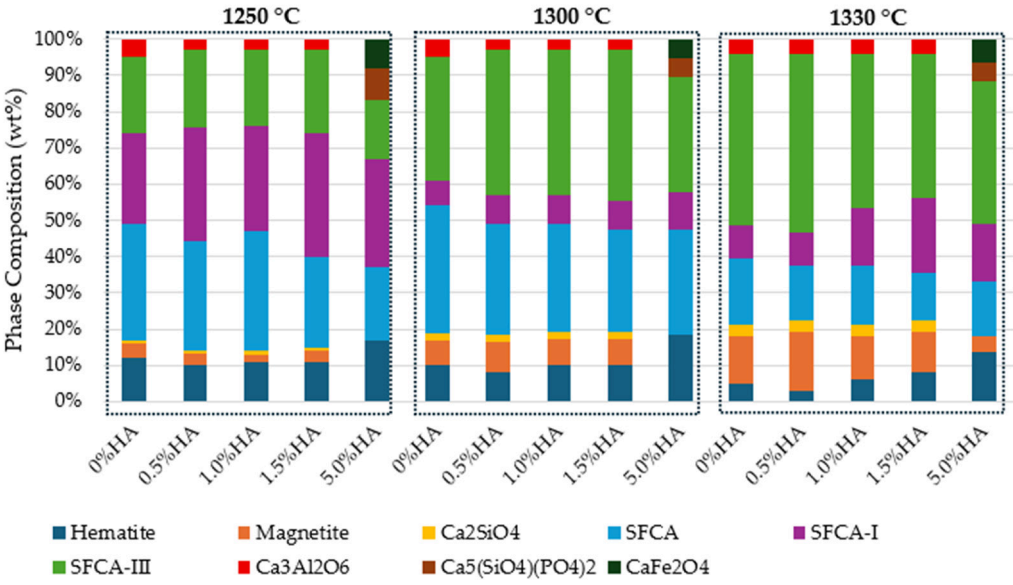


Figure 4. Results of Rietveld-based QXRD analysis of SA blend samples.

At 1250 °C, hematite and SFCA phases were the dominant phases present, together accounting for more than 80 wt.% of the total composition. Of the SFCA phases present, SFCA (~15–33 wt.%) was the dominant type, with SFCA-III the next most prominent (~14–17 wt.%) and SFCA-I present in smaller amounts (~6–7 wt.%). The presence of significant amounts of SFCA and hematite (~37–69 wt.%) and a smaller amount of SFCA-I is consistent with the results of Webster et al. [20], which indicated that SFCA is stable at higher temperatures than SFCA-I. In general, progressive HA addition up to 1.5 wt.% had little influence on the overall phase assemblage; however, at the addition level of 5.0 wt.% HA, several notable changes were observed. In this sample, SFCA-I and SFCA-III phase formation was suppressed and the amount of SFCA decreased to about 15 wt.%. In addition, the hematite content increased significantly to ~70 wt.%, the magnetite content virtually disappeared (~1 wt.%) and formation of the $Ca_5(SiO_4)(PO_4)_2$ phase (~4 wt.%) occurred, indicating the incorporation of P into Ca–Si-rich compounds. Furthermore, $Ca_2Fe_2O_5$, which formed at low temperatures through the initial reaction between CaO and Fe_2O_3 and serves as a precursor to more complex calcium ferrite and silicate phases [20], was

present at approximately 9 wt.% in the 5 wt.% HA sample but was not observed at lower HA additions. Therefore, it appears that the presence of high levels of P in the JSM blend suppresses or delays the 'SFCA' bonding phase formation. This observation is consistent with the lower strength observed for the 5 wt.% HA sample at 1250 °C (Figure 1).

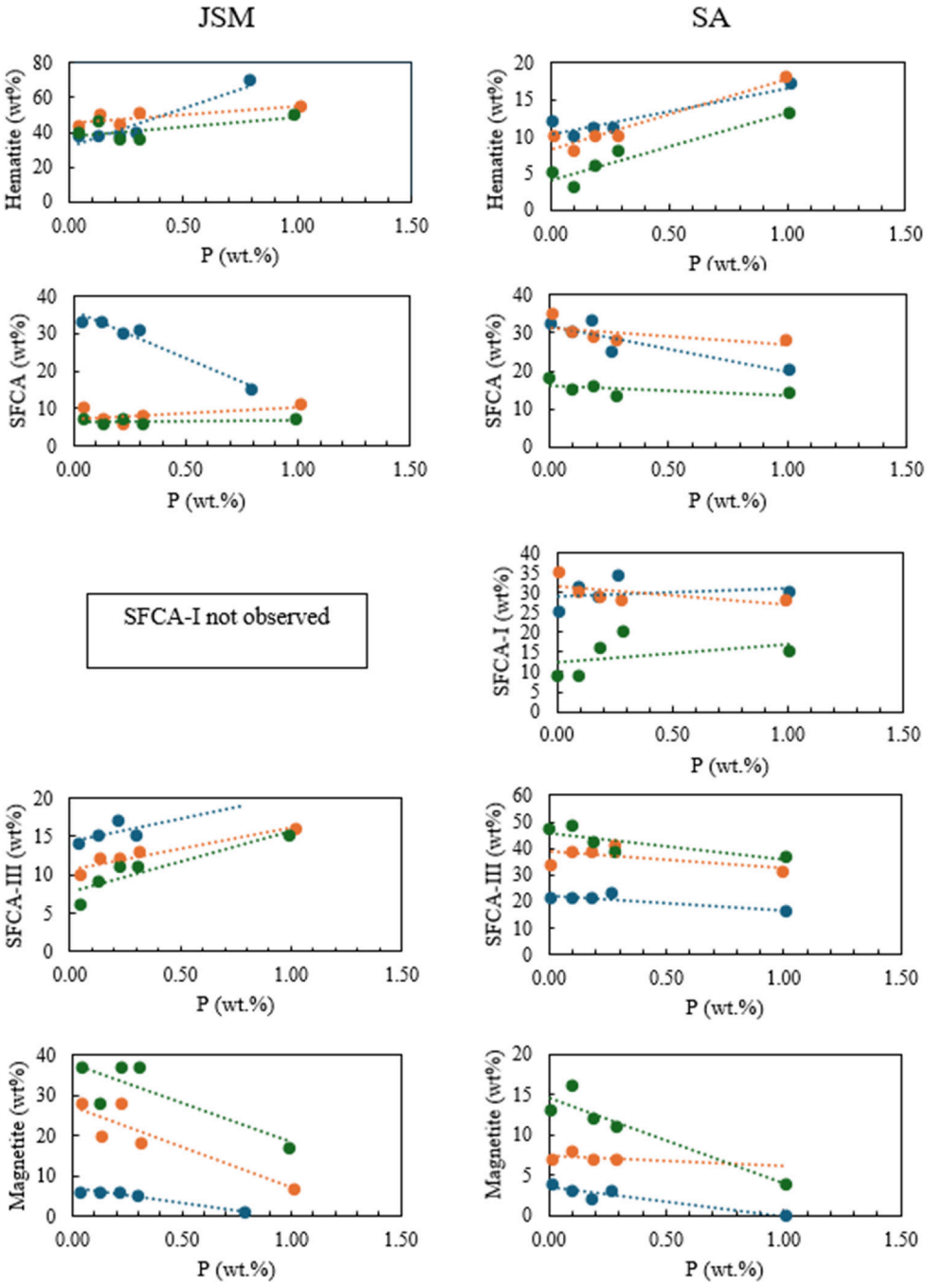


Figure 5. Relationship between P content and main phases formed during sintering using JSM (**left**) and SA (**right**) samples. Note that these plots are derived from the same Rietveld-based QXRD dataset shown in Figures 3 and 4, replotted against measured wt.% P (from XRF) rather than wt.% HA addition. Blue dots = 1250 °C; orange dots = 1300 °C and green dots = 1330 °C.

At 1300 °C, the proportion of SFCA decreased markedly to <10 wt.% in the samples with up to 1.5 wt.% HA addition, while SFCA-I was not present in any sample. SFCA-III was, however, present in all samples up to 1.5 wt.% HA addition at a constant level of ~10–13 wt.%. The decrease in the total amount of 'SFCA' phases occurred at the expense of

increased hematite and magnetite, which together became the dominant phases (>70 wt.%) in compositions up to 1.5 wt.% HA. An increase in temperature from 1250 °C to 1300 °C also promoted the increased formation of larnite (Ca_2SiO_4), with an average level of ~9–10 wt.% across all composition up to 1.5 wt.% HA. While the amounts of SFCA and SFCA-III remained relatively constant across all samples up to 1.5 wt.% HA addition, in the experiment containing 5 wt.% HA, there was a noticeable increase in both SFCA-III (~16 wt.%) and SFCA (~11 wt.%) formation. There was, however, a notable decrease in the magnetite content, with only ~7 wt.% present. The decrease in magnetite content appears to be at the expense of the increase in total 'SFCA' phases and slightly more hematite. The amount of larnite was lowest in the 5.0 wt.% HA experiment, which was likely due to the formation of the $Ca_5(SiO_4)(PO_4)_2$ phase. Furthermore, the $Ca_2Fe_2O_5$ phase was low in the high-P sample (~1 wt.%), presumably due to the higher temperature leading to the formation of more 'SFCA' phases.

At 1330 °C, the results up to 1.5% HA addition were like those at 1300 °C. Notable differences included magnetite and hematite as the dominant phases, together exceeding 75 wt.%, while both SFCA (~6–7 wt.%) and SFCA-III (~6–11 wt.%) were present at their lowest levels. The increase in the magnetite phase compared to the lower temperature experiments is consistent with previous in situ XRD results from Webster et al. [21], which showed that as temperatures approached the melting point of the system, there was an increase in the amount of magnetite that formed. Larnite continued to be present at constant levels of ~9–10 wt.%. At the highest HA addition, results were also like those from the 1300 °C data. The amount of SFCA-III remained the same as observed in the lower temperature data; however, SFCA, $Ca_5(SiO_4)(PO_4)_2$ and hematite all showed a slight decrease at the expense of increased magnetite.

Overall, for the JSM blend samples, the XRD results indicate that temperature and P addition both strongly influence phase evolution during sintering. In general, as the temperature increased from 1250 to 1330 °C, SFCA and SFCA-I progressively became destabilized, resulting in increased magnetite and hematite (Figure 5). SFCA-III remained relatively constant across all temperatures and compositions, except for the lowest temperature 5.0% HA composition where SFCA-III was not observed. Higher temperatures favored the formation of larnite, and excessive P addition (5.0 wt.% HA) promoted the formation of Ca–Si–P compounds such as $Ca_5(SiO_4)(PO_4)_2$. The results show that P preferentially reacts with Ca and Si at high temperatures, modifying the equilibrium between 'SFCA' and silicate phases.

SA Samples

The QXRD results for the SA blend sinter samples synthesized at 1250 °C, 1300 °C, and 1330 °C and with varying HA additions (0–5 wt.%) are shown in Figure 4. Across all temperatures, the main crystalline phases identified were hematite, magnetite, SFCA-type phases (SFCA, SFCA-I, and SFCA-III), tricalcium aluminate ($Ca_3Al_2O_6$), larnite (Ca_2SiO_4), and, in lower amounts, calcium-ferrite ($CaFe_2O4$) and silico-phosphate ($Ca_5(SiO_4)(PO_4)_2$).

At 1250 °C in compositions with up to 1.5% HA addition, 'SFCA' phases (SFCA, SFCA-I, and SFCA-III) dominated the phase assemblage, collectively accounting for approximately 80 wt.% of the total composition. Compared to the JSM blend, there were significantly more total 'SFCA' phases formed and less hematite and magnetite, consistent with the composition being designed to maximize SFCA phases. The calcium aluminate phase, $Ca_3Al_2O_6$, was present at levels up to 5 wt.%, and its formation in synthetic sinter compositions was previously noted by Webster et al. [20]. Larnite formation was minimal (<1 wt.%). The gradual addition of HA up to 1.5 wt.% therefore had minimal effect on the overall phase balance between samples (Figure 4). However, at the higher addition

level of 5.0 wt.% HA, significant changes were observed. 'SFCA' phases decreased in total abundance and both the larnite and $Ca_3Al_2O_6$ phases disappeared to form new phases such as $CaFe_2O_4$ and $Ca_5(SiO_4)(PO_4)_2$ (both at ~8–9 wt.%).

As the temperature was increased to 1300 °C, SFCA-I became less stable and there was a significant increase in the amount of SFCA-III formed. The proportions of other phases showed minimal variation with the increase in temperature to 1300 °C, except in the sample containing 5 wt.% HA, where larnite and magnetite were no longer detected and there was an increase in the amount of magnetite and formation of $CaFe_2O_4$ and $Ca_5(SiO_4)(PO_4)_2$.

At the highest temperature of 1330 °C, a distinct change in the evolution of SFCA-type phases was noted. In samples with low HA additions (up to 0.5 wt.%), the SFCA decreased, whereas the amount of SFCA-III formed increased. With higher HA additions (≥1.0 wt.%), the formation of SFCA-III was suppressed, favoring the stabilization of SFCA-I. This observation was unexpected as SFCA-I is usually only stable below 1300 °C, suggesting that for compositions close to the stability region where SFCA phases form, the presence of P promotes an increase in its stability to higher temperatures. In the sample containing 5 wt.% HA, the total amount of 'SFCA' phases was slightly reduced and larnite was no longer detected. Similar to the same sample run at 1250 °C, the amount of hematite increased and there was a decrease in the amount of magnetite and formation of $CaFe_2O_4$ and $Ca_5(SiO_4)(PO_4)_2$.

In the SA blend, similar trends were observed, though with generally lower hematite levels compared to the JSM samples. Like what was observed in the JSM samples, the results for the SA blend samples confirm that temperature and P addition significantly influence the stability and transformation pathways of SFCA-type phases. As temperature increased, SFCA-I progressively became destabilized and converted to SFCA-III, followed by partial decomposition of SFCA at the highest temperature. However, unlike the JSM blend, the SA samples exhibited a decline in SFCA-III with rising P content. Magnetite also declined with increasing P, though less sharply than in the JSM samples. In summary, within each temperature series, moderate HA additions (≤1.5 wt.%) caused only minor changes in phase proportions, whereas excessive addition (5 wt.% HA) disrupted the equilibrium between ferrite and silicate phases, promoting the formation of Ca–Fe and Ca–Si–P compounds and altering the distribution of iron oxides and 'SFCA' phases.

3.2.2. Microstructural Evolution and Pore Formation

The microstructural characteristics of the sinter samples provide valuable insights into the phase transformations and textural development occurring during heating, particularly under the influence of P addition. Figure 6 and Figure 7 illustrate the reflected light micrographs of the JSM and SA blends under varying temperatures and P sources, respectively. These images allow for a visual qualitative comparative assessment of how the P source, concentration, and temperature collectively influence melt formation, phase distribution, and pore development within the sintered matrix.

For the JSM samples (Figure 6) fired at 1250 °C, limited melt is produced regardless of P content, resulting in poorly bonded structures dominated by hematite, with some SFCA and minimal SFCA-I formation. At this temperature, pores are irregular and poorly connected, and although individual pores can be large in section, they are on average smaller than those observed at 1300 and 1330 °C, reflecting the more limited melt formation at this temperature; increasing P has little observable effect at this stage. At 1300 °C, pore rounding becomes evident due to increased melt formation. Hematite remains the dominant phase; however, bonding phases such as SFCA and some magnetite are also observed. With increasing P, pores become larger and more spherical, indicating enhanced liquid mobility and gas entrapment, and the pore distribution becomes less uniform at higher P levels (e.g., 5% HA).

At 1330 °C, pore coarsening is pronounced, with large, spherical pores dominating at most P levels. However, at the highest P content, pores appear somewhat reduced in size and more irregular in shape. Additionally, the morphology of SFCA becomes less distinct at higher P levels.

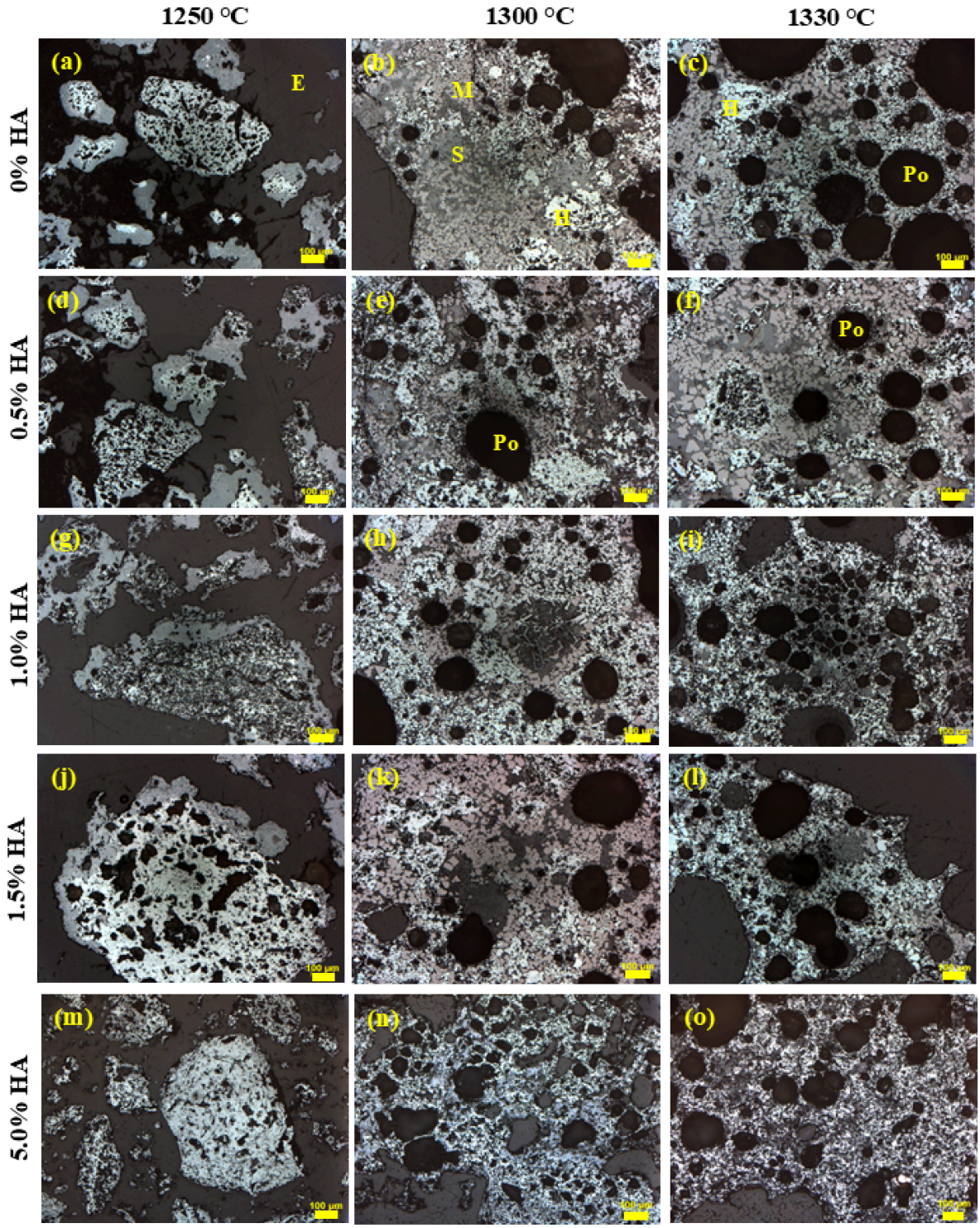


Figure 6. Reflective light plane polarized photomicrographs showing the microstructural evolution and pore formation of the JSM blend sinter samples. Magnification ×200. H = hematite, M = magnetite, S = SFCA, Po = pores (solid black areas), and E = epoxy (solid dark grey areas). Scale bar in each image is 100 microns.

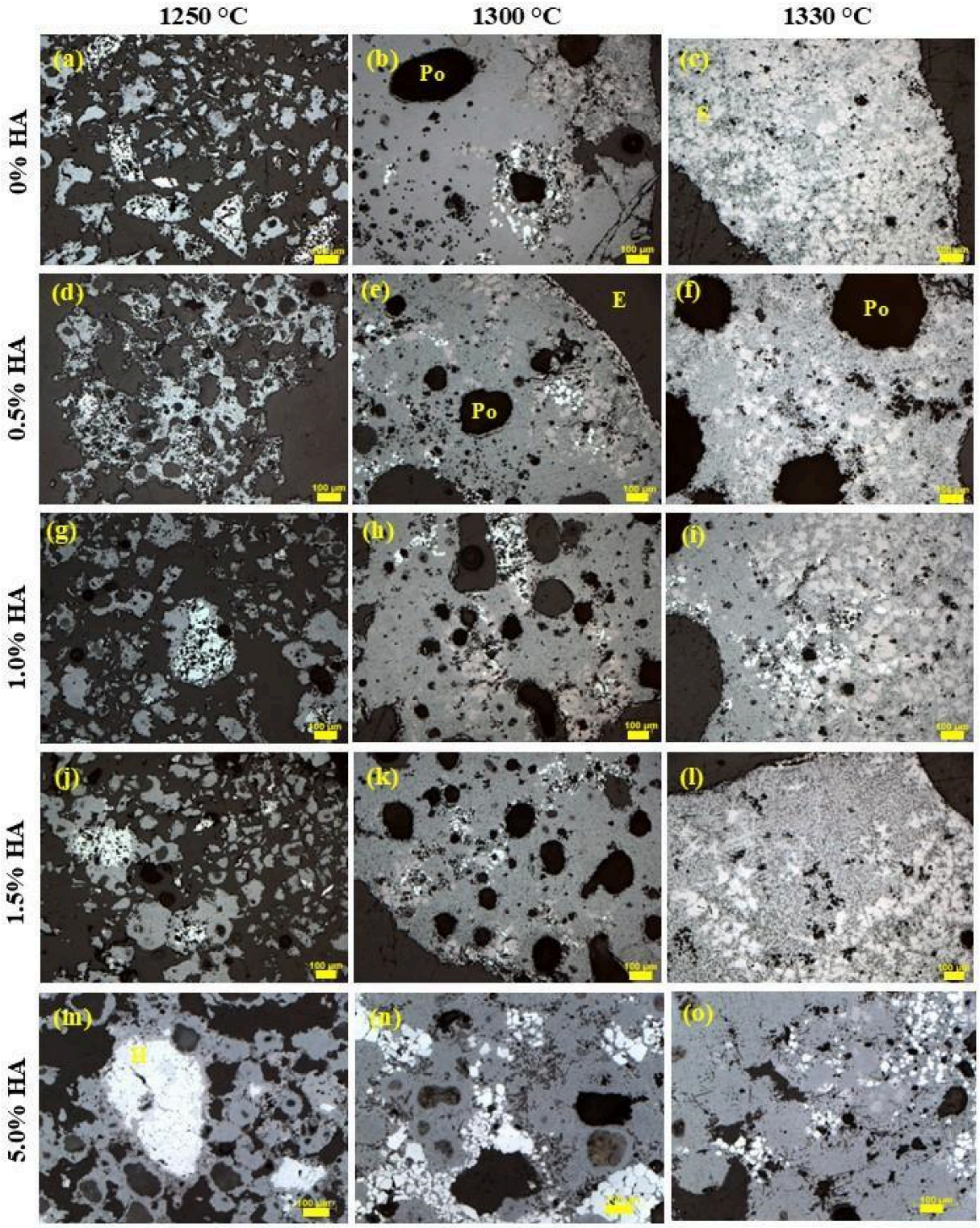


Figure 7. Reflective light plane polarized photomicrographs showing the microstructural evolution and pore formation of the SA blend sinter samples. Magnification ×200. H = hematite, M = magnetite, S = SFCA, Po = pores (solid black areas), and E = epoxy (solid dark grey areas). Scale bar in each image is 200 microns.

For the SA samples (Figure 7), the combined influence of temperature and P addition again controls melt formation, phase development, and pore evolution, although the response differs from the JSM blend. At 1250 °C, melt formation is limited across all P levels, resulting in a heterogeneous and weakly bonded solid structure dominated by

SFCA with minor hematite. Pores are irregular, fine, and poorly connected, and increasing P has minimal effect on the overall morphology, although slightly more intergranular material appears at higher P additions. At 1300 °C, a significant increase in melting leads to improved bonding and noticeable pore rounding. SFCA phases act as the primary bonding phase, with hematite becoming more apparent at higher P levels (e.g., 5% HA). At higher P levels (≥1.5% HA), pore coalescence becomes more evident, and the bonding solid structure appears less uniform. At 1330 °C, extensive melt formation produces a dense, homogenized matrix. The pores are much smaller and more uniformly distributed throughout the sample. However, at 0.5% HA and 5% HA, the structure appears more heterogeneous, with irregular pore shapes and possible phase segregation. Additionally, the distinction of SFCA becomes less clear at higher P levels, suggesting that P-rich melt alters phase stability and solidification behavior. Overall, P acts as a flux, enhancing melt formation. At the highest P addition, this is accompanied by a degree of pore coarsening and a less well-defined bonding phase morphology at high temperature, although this trend is subtle and not observed uniformly across all compositions.

The pore descriptions above are based on qualitative visual assessments of the micrographs; quantitative image analysis of pore size distribution and connectivity was outside the scope of this study but would allow the observed microstructural trends to be more directly correlated with the tumble index strength results in Section 3.1.

3.2.3. Phosphorus Distribution

Figure 8 presents a representative backscattered electron (BSE) image of the sinter analogue sample containing 1.5 wt.% HA addition (sample SA 1.5% HA), highlighting three regions selected for detailed microstructural and compositional analysis (Regions 1–3). Each region corresponds to distinct microstructural features observed within the sintered matrix, including iron oxide grains, bonding phases, and glassy areas.

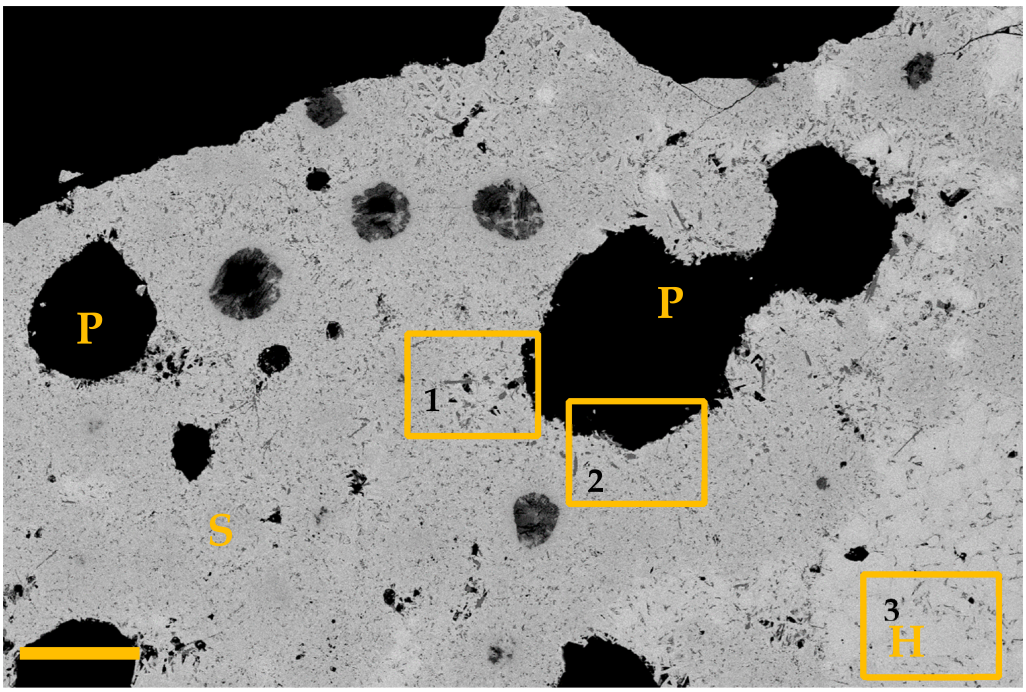
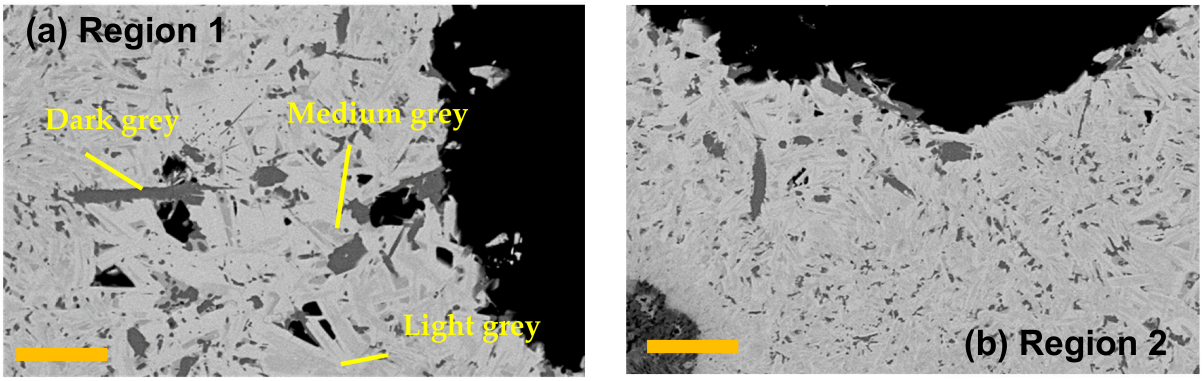


Figure 8. Backscattered electron image of SA 1.5% HA fired at 1300 °C showing three regions of interest. Region 3 is dominated by hematite (bright, white phase), whereas Regions 1 and 2 comprise 'SFCA' and P-rich phases. Regions 1 and 2 are shown in detail in Figure 9. Scale bar is equal to 100 microns. H = hematite, P = pore, S = SFCA (undifferentiated).



Average (wt.%)	Fe	O	P	Ca	Al	Si	Phase
Dark grey	5.8	42	13	35	0.26	4.1	*P-substituted larnite or $Ca_5(SiO_4)(PO_4)_2$
Medium grey	48	33	0.01	14	3.5	1. 9	'SFCA'
Light grey	54	32	0.02	9.7	3.0	1.1	'SFCA'

*The identification of P-substituted larnite or $Ca_5(SiO_4)(PO_4)_2$is difficult based on chemistry alone.

Figure 9. High-resolution BSE images and standardless SEM-EDS analysis results from phases within (**a**) Region 1 and (**b**) Region 2 (see Figure 8 for locations). Scale bar in each image is 10 microns. Note that 'SFCA' is used here to refer collectively to the SFCA-type phases (SFCA, SFCA-I, SFCA-III), which could not be reliably distinguished from one another by SEM-EDS due to their fine-scale intergrowth and closely overlapping compositions.

Region 1 (Figure 9a) corresponds to a calcium silicate-enriched area embedded within an iron-rich bonding phase composed of coarse-grained SFCA. The dark grey areas show high Ca (≈33–36 wt.%), Si (≈3–5.5 wt.%) and P (≈10–14 wt.%), along with relatively low Fe (≈5–8 wt.%), consistent with the presence of P-rich and associated glassy phases. In contrast, the light grey areas exhibit high Fe (≈51–58 wt.%) and Al (≈2–4 wt.%) and lower Ca (≈8–12 wt.%) and Si (≈0.6–1.6 wt.%), typical of SFCA-type intergrowths but with no detectable P. Note there is considerable chemical zonation within the SFCA phase, which typically exhibits darker (Fe-poor) cores and lighter rims (Fe-rich). This type of zonation is commonly observed in industrially prepared iron sinters and reflects the non-equilibrium conditions of the sintering process. The results confirm that P was mainly concentrated in the P-rich (lenticular-shaped dark grey phase) and possibly other glassy phases rather than within the SFCA matrix.

Region 2 (Figure 9b) represents an area dominated by SFCA-I (fine microplaty variant of SFCA) interspersed with P-rich and glass phases. Like Region 1, P was detected exclusively within the Ca–Si-rich areas (dark grey), confirming a consistent trend of P segregation into these phases rather than incorporation into the Fe-rich bonding matrix phase.

Region 3 corresponds to a high-Fe area composed mainly of SFCA-I (fine microplaty, grey contrast phase) together with hematite (bright phase). The SFCA-I platelets were small and highly zoned and not suitable for reliable spectrum acquisition; therefore, all EDS analysis results were collected from the bright areas which were Fe-rich, most likely hematite. No P was detected in hematite.

Overall, these observations indicate that at a 1.5 wt.% HA addition, P preferentially reacts with CaO and SiO_2, promoting the formation of P-rich and glassy phases rather than being incorporated into the silico-ferrite matrix (SFCA/SFCA-I) and hematite phases.

This selective association suggests that HA-derived P contributes to phase segregation, potentially influencing the bonding strength and overall sinter structure.

The two high-temperature samples JSM 1.5% HA and SA 1.5% HA were mapped using the electron microprobe to examine the distribution of P. Results are shown in Figure 10 in the form of a WDS elemental X-ray map showing the distribution of P within the mapped area together with a phase distribution map showing the chemistry of the major phases present.

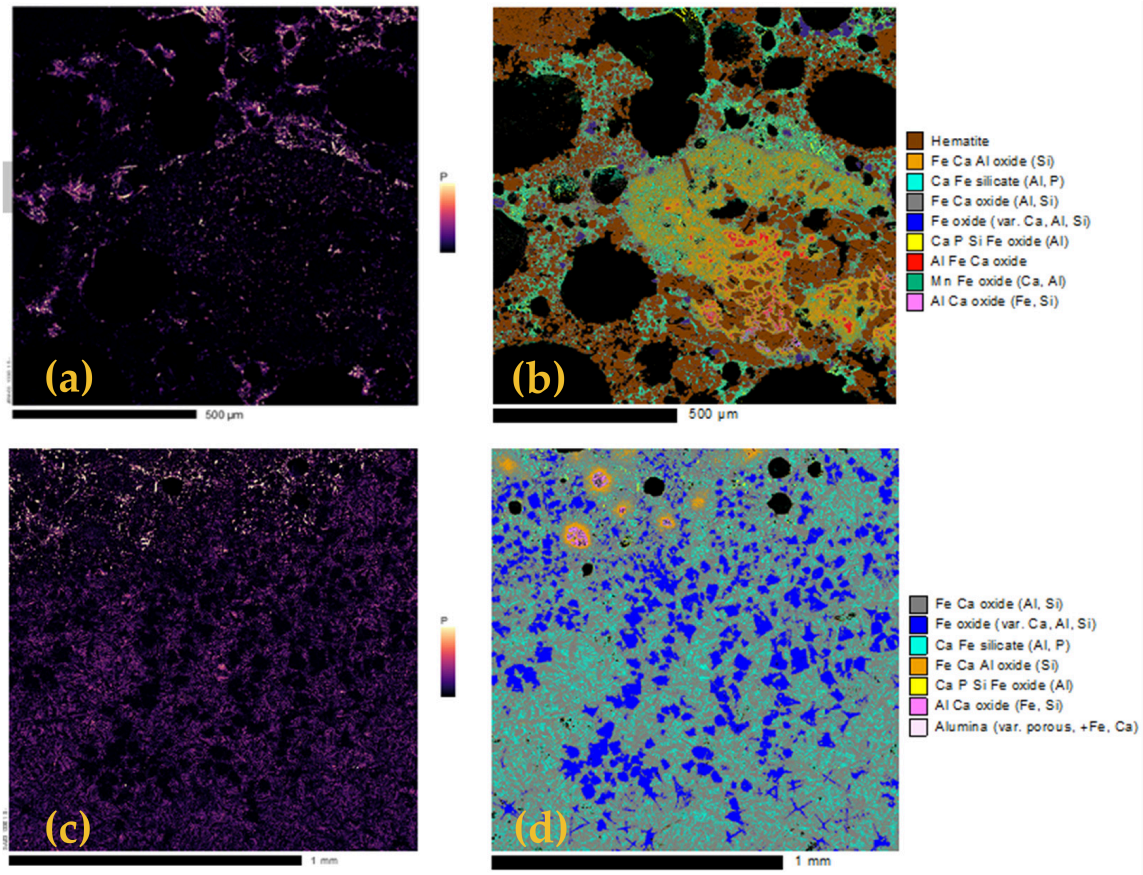


Figure 10. EPMA map results showing the P distribution and clustered phase map for samples JSM 1330 °C, 1.5% HA (**a**,**b**) and SA 1330 °C, 1.5% HA (**c**,**d**). The nomenclature of phases is based on major element chemistry, as the composition of few phases approached the stoichiometric ideal for expected phases.

The JSM sample (1330 °C, 1.5% HA) shown in Figure 10a,b covers a region dominated by high amounts of hematite, high porosity and a complex assemblage of various Fe/Ca/Al/Si oxide phases. The latter phases represent the complex chemistries exhibited by Ca-ferrite and 'SFCA' phases, and it is not possible to ascribe a unique mineral identification to these phases (e.g., SFCA, SFCA-I etc.) as high magnification shows the material is highly zoned—see also Figure 9a where the individual 'SFCA' crystals have darker cores and lighter rims indicating strong chemical zonation—presumably due to the rapid 3 min reaction time leading to non-equilibrium phases being formed. For this reason, the phases that are identifiable as distinct chemical phases have not been named but instead labeled based on their major element chemistry.

The major P-bearing phase in the mapped area of the JSM sample is present at the level of ~2%–3% (by area) and is labeled as 'Ca P Si Fe oxide', which also contains minor to trace Al. It appears to form long elongated needle-like (in 2D section) crystals with an average composition of 36% Ca, 7% Fe, 5% Si, 10% P and 0.3% Al (as weight percent), like

that of the 'dark grey' phase identified by SEM-EDS (Figure 9). This phase is most likely a highly P-substituted larnite phase or alternatively a $Ca_5(SiO_4)(PO_4)_2$ phase (silicocarnotite) which has a nominal composition of 42% Ca, 6% Si, and 13% P. The P-rich phase is mainly present in close association with a Ca Fe silicate (Al, P) phase. The latter phase represents ~10% of the area mapped, with an average composition of 29% Ca, 26% Fe, 7% Si, 2% Al and ~1% P. Based on the composition it is possible this is a type of 'SFCA', although it is unclear whether it is SFCA or SFCA-III, but it may also represent a fine intergrowth of two or more phases, resulting in a non-stoichiometric average composition.

The mapped area from the SA sample shown in Figure 10c,d is from a region dominated by magnetite and the same Ca Fe silicate (Al, P) and Fe Ca oxide (Al, Si) phases present in the JSM sample. The Ca Fe silicate (Al, P) phase again has an 'SFCA'-like composition, and based on the XRD data (Figure 4) it most likely represents SFCA-III, the most dominant 'SFCA' phase in the sample. Note that the high aluminum areas in the upper part of the map (Figure 10d) appear to be residual, un- or partially reacted alumina, as well as Al-Ca oxides.

The SEM and EPMA results indicate that P is concentrated primarily in three phases in the sinter samples. The most P is incorporated in $Ca_5(SiO_4)(PO_4)_2$ phases (Figures 9 and 10); however, the EPMA mapping suggests that a minor amount of P may be incorporated in 'SFCA' (or a phase intergrown with SFCA) at high temperatures. The preliminary evidence suggests this is likely to be in SFCA-III; however, further work is needed to verify this hypothesis. This analysis also suggests that the samples had not reached equilibrium, as evidenced by large-scale diffusion gradients (particularly for Al), significant heterogeneity in the phase assemblages within the maps, and abundance differences between the two specimens.

3.2.4. In Situ XRD

In situ XRD data were obtained for the two SA and JSM samples, each containing 1.5% HA. This addition level was selected as it still produces a phase assemblage broadly similar to the P-free system (Section 3.2.1), allowing a direct test of whether a moderate P level affects the sequence or temperature of SFCA-type phase formation and decomposition; the more complex, multi-phase assemblage formed at 5 wt.% HA would be difficult to resolve unambiguously from in situ XRD data due to peak overlap and is left for future work. There is previous in situ XRD data for the P-free SA sample [20,30]; however, the data for the JSM blend is new and represents the first time a 'real' sinter blend composition has been analyzed by the in situ XRD technique.

Figure 11 shows the plot of accumulated in situ XRD data in the range of 298 to 1623 K (≈25 and 1350 °C) at $pO_2 = 5 \times 10^{-3}$ atm collected for the (a) JSM blend sample containing 1.5 wt.% HA and (b) the SA sample containing 1.5 wt.% HA over the range $5° < 2\theta < 50°$. The sequence of phase decomposition/formation events during heating was: decomposition of $Al(OH)_3$; decomposition of $CaCO_3$ and formation of CaO; formation of C2F (i.e., dicalcium ferrite, $Ca_2Fe_2O_5$); formation of CF (i.e., calcium ferrite, $CaFe_2O_4$); and formation of SFCA-I (nominal composition $Ca_{3.2}Fe_{2+0.8}Fe_{3+14.7}Al_{1.3}O_{28}$) and SFCA (nominal composition $Ca_{2.3}Mg_{0.8}Si_{1.1}Al_{1.5}Fe_{8.3}O_{20}$). In (a), quartz peaks were observed and the α to β transition was observed at ~600 °C. In (a), above 1250 °C the SFCA-I and SFCA had decomposed and the phase assemblage was Fe_3O_4 in a Fe_2O_3(FeO)—CaO—SiO_2 melt, and in (b), above 1275 °C the SFCA-I and SFCA had decomposed to form the same phase assemblage. The higher melting point of the SA mixture is consistent with its higher Al_2O_3 content [20].

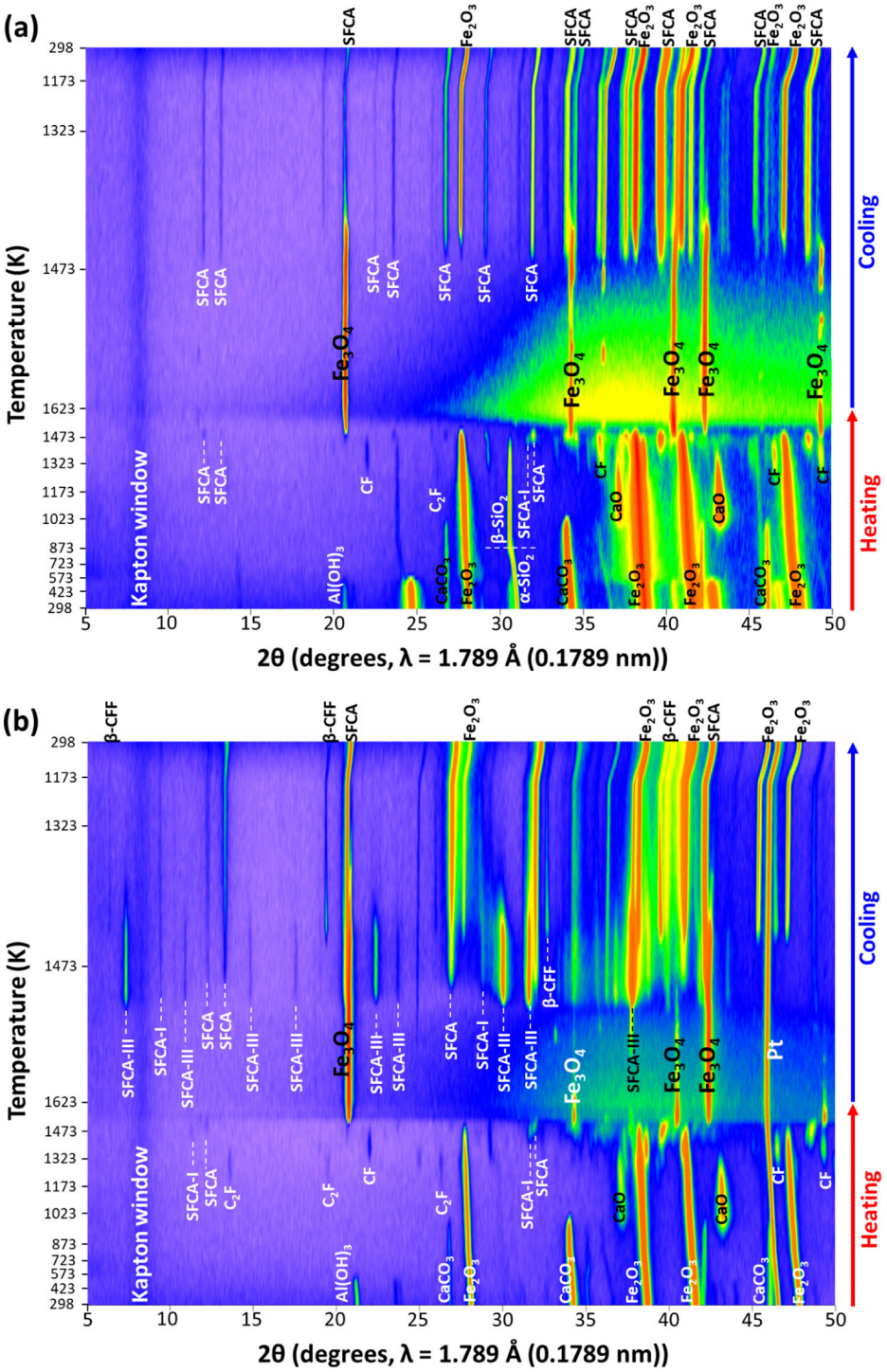


Figure 11. In situ XRD data collected during heating and cooling of (**a**) the JSM blend sample containing 1.5% HA and (**b**) the SA sample containing 1.5% HA in the range 25–1350 °C at $pO_2 = 5 \times 10^{-3}$ atm. The broad peak at ~8° 2θ is scatter from the Kapton window of the Anton Paar chamber. The colors represent the intensity of the peaks, from purple (lowest intensity, background) to blue, green, yellow, and red (highest intensity).

During cooling, in (a) for the JSM blend, the first phase to crystallize from the melt was SFCA below 1200 °C, and below 1190 °C the magnetite began to oxidize to hematite, and this oxidation was complete by 1120 °C. The lack of SFCA-III formation for this mixture with basicity = 2.2 under these experimental conditions is consistent with the previous in situ XRD results of Webster et al. [31], where it was shown that as the basicity decreased, the formation of SFCA-III/Fe-rich SFCA was suppressed. In (b) for the SA mixture, SFCA-

III was the first phase to crystallize from the melt at 1250 °C, followed by SFCA-I and SFCA within a few degrees thereafter. Under the cooling conditions used (2 °C min^{-1}, pO_2 = 0.005 atm), the SFCA-III phase does not persist to ambient temperature, whilst SFCA and SFCA-I remain [30]. Below 1175 °C the magnetite began to oxidize to hematite, and this oxidation was completed by 1090 °C; the stabilization of magnetite to lower temperature than for the JSM blend sample is again consistent with the higher Al_2O_3 concentration of the SA sample.

Based on the QXRD results in Figures 3 and 4, it was not anticipated that the in situ XRD analysis would reveal any P-rich phases due to the low amount of P added. However, the results confirm that the effect of P on phase formation is minimal, as the sequence of SFCA-I and SFCA-III phase formation in the SA blend was identical to that observed by Webster et al. [30] for the equivalent P-free sample. This observation is also consistent with the EDS results in Figure 9, which suggest that the 'SFCA' phases do not preferentially take P into their structure, and hence their formation and stability are not affected by the presence of P. Although in situ data for P-free JSM samples is not available, it is also likely that low levels of P have no effect on SFCA phase stability.

4. Conclusions

This study examines, at the laboratory scale, the influence of P on phase formation during sintering and the resulting implications for phase stability and sinter quality. These effects were examined under two complementary conditions: an industrially representative blend of natural iron ores and a synthetic high-purity system designed to promote SFCA formation and allow controlled assessment of phase stability. Phosphorus was introduced at varying concentrations in both systems to systematically evaluate its role during sintering.

All P-doped JSM samples fired within the temperature range of 1300 to 1330 °C met the minimum strength requirement (TI = 80%) for producing high-quality sinters. In the case of the SA mixture, samples showed an improvement in TI strength from 1250 to 1300 °C, although the enhancement in strength was not as pronounced as in the JSM samples. A key distinction between the SA and JSM blend samples was that the SA samples displayed notably greater strength at 1250 °C. Nevertheless, in contrast to the JSM samples, the SA samples peaked in strength at 1300 °C and then experienced a slight decrease in strength at temperatures exceeding 1300 °C. A more substantial reduction was noted in the high-P composition (5 wt.% HA), suggesting that higher P content diminishes strength at elevated temperatures—at least in the synthetic SA sample.

Examination using XRD revealed that adding small to medium amounts of HA ($\leq$1.5 wt.%) had a limited impact on the overall mineral phases and did not notably disturb the formation of the 'SFCA' bonding phases. Conversely, adding a high amount of HA (5 wt.%) encouraged the creation of Ca–Si–P phases. Analysis of the microstructure, minerals, and microchemistry indicated that P tends to segregate phases rich in phosphate by interacting with calcium oxide and silica. Note, however, that a semi-quantitative chemical assessment of the SFCA-III phase by EDS indicates that a small quantity of P might be able to be integrated into the structure; this remains an inconclusive, preliminary observation and needs validation through more precise EPMA analyses. In situ XRD results obtained in the presence of 1.5% HA in the SA and JSM samples showed that, for the SA sample, there was no noticeable impact on phase formation when compared to a similar system without P. While there is no comparable in situ data available for the P-free JSM sample, it is probable that low levels of phosphorus do not affect the stability of 'SFCA' phases.

Overall, the findings from this study provide direct evidence that, at the levels of P typically found in iron ores, sinter strength and SFCA phase stability are largely preserved, supporting the potential use of high-P ores in sinter blends.

Author Contributions: Conceptualization, I.R.I., M.I.P.; methodology, I.R.I., M.I.P., N.A.W., N.A.S.W., A.T.; investigation, I.R.I., M.I.P.; resources, M.I.P.; data curation, I.R.I.; writing—original draft preparation, I.R.I.; writing—review and editing, I.R.I., M.I.P., N.A.W., N.A.S.W., A.T.; visualization, I.R.I., N.A.S.W., A.T.; supervision, M.I.P. All authors have read and agreed to the published version of the manuscript.

Funding: This research received no external funding.

Data Availability Statement: The original contributions presented in this study are included in the article. Further inquiries can be directed to the corresponding author.

Acknowledgments: The authors acknowledge the contributions of Nick Wilson (CSIRO Mineral Resources, Clayton) for EPMA method development and operation, Cameron Davidson (CSIRO Mineral Resources) for SEM and EPMA specimen preparation, Steve Peacock (CSIRO Mineral Resources, Clayton) for XRF specimen preparation, data collection and analysis, James Manuel (CSIRO Mineral Resources, Pullenvale) for his optical image analysis discussions, and Rodrigo Gomez-Camacho (CSIRO Mineral Resources, Waite) for XRD sample preparation and data collection. The authors gratefully acknowledge funding from ARC LE130100087 to purchase the EPMA.

Conflicts of Interest: The authors declare no conflicts of interest.

References

1. Nicol, S.; Chen, J.; Pownceby, M.I.; Webster, N.A.S. A review of the chemistry, structure and formation conditions of silico-ferrite of calcium and aluminum ('SFCA') phases. *ISIJ Int.* **2018**, *58*, 2157–2172. [CrossRef]
2. Potter, N.J.; Clout, J.M.F.; Brand, N.W. Spatial distribution of major, minor and trace elements in iron ores, using micro-XRF technology. In *Proceedings of the Iron Ore Conference, Perth, WA, Australia, 8–10 November 2021*; The Australasian Institute of Mining and Metallurgy: Melbourne, Australia, 2021; pp. 417–427.
3. Pownceby, M.I.; Hapugoda, S.; Manuel, J.; Webster, N.A.S.; MacRae, C.M. Characterisation of phosphorus and other impurities in goethite-rich iron ores—Possible P incorporation mechanisms. *Miner. Eng.* **2019**, *143*, 106022. [CrossRef]
4. Dukino, R.D.; England, B.M.; Kneeshaw, M. Phosphorus distribution in BIF-derived iron ores of Hamersley Province, Western Australia. *Trans. Inst. Min. Metall. Sect. C Appl. Earth Sci.* **2000**, *109*, 168–176. [CrossRef]
5. Krautschick, H.J.; Grabke, H.J.; Diekmann, W. The effect of phosphorus on the mechanism of intergranular stress corrosion cracking of mild steels in nitrate solutions. *Corros. Sci.* **1988**, *28*, 251–258. [CrossRef]
6. Ji, G.; Gao, X.; Sohn, I.L.; Ueda, S.; Wang, W. Review of beneficiation techniques and new thinking for comprehensive utilization of high-phosphorus iron ores. *Miner. Eng.* **2025**, *223*, 109176. [CrossRef]
7. Holmes, R.J.; Lu, L. Introduction: Overview of the global iron ore industry. In *Iron Ore: Mineralogy, Processing and Environmental Sustainability*; Elsevier Inc.: Amsterdam, The Netherlands, 2015; pp. 1–42. [CrossRef]
8. Xue, X.M.; Jiang, H.G.; Sui, Z.T.; Ding, B.Z.; Hu, Z.Q. Influence of phosphorus addition on the surface tension of liquid iron and segregation of phosphorus on the surface of Fe-P alloy. *Metall. Mater. Trans. B* **1996**, *27*, 71–79. [CrossRef]
9. Patrick, T.R.C.; Lovel, R.R. Leaching dicalcium silicates from iron ore sinter to remove phosphorus and other contaminants. *ISIJ Int.* **2001**, *41*, 128–135. [CrossRef]
10. MacRae, C.; Wilson, N.; Pownceby, M.; Miller, P. Phosphorus and other impurities in Australian iron ores. *Microsc. Microanal.* **2010**, *16*, 896–897. [CrossRef]
11. Ofoegbu, S.U. Technological challenges of phosphorus removal in high-phosphorus ores: Sustainability implications and possibilities for greener ore processing. *Sustainability* **2019**, *11*, 6787. [CrossRef]
12. Singh, A.; Singh, V.; Patra, S.; Dixit, P.; Mukherjee, A.K. Review on high phosphorous in iron ore: Problem and way out. *Min. Metall. Explor.* **2024**, *41*, 1497–1507. [CrossRef]
13. Clout, J.M.F.; Manuel, J.R. Fundamental investigations of differences in bonding mechanisms in iron ore sinter formed from magnetite concentrates and hematite ores. *Powder Technol.* **2003**, *130*, 393–399. [CrossRef]
14. Lu, L.; Adam, M.; Kilburn, M.; Hapugoda, S.; Somerville, M.; Jahanshahi, S.; Mathieson, J.G. Substitution of charcoal for coke breeze in iron ore sintering. *ISIJ Int.* **2013**, *53*, 1607–1616. [CrossRef]
15. Ware, N.; Manuel, J. Fundamental nucleus assimilation behaviour of haematite and goethite containing ores in iron ore sintering. *Trans. Inst. Min. Metall. Sect. C Miner. Process. Extr. Metall.* **2016**, *125*, 149–155. [CrossRef]
16. Umadevi, T.; Sah, R.; Mahapatra, P.C. Influence of sinter basicity (CaO/SiO_2) on low and high alumina iron ore sinter quality. *Miner. Process. Extr. Metall.* **2014**, *123*, 75–85. [CrossRef]

17. Pownceby, M.I.; Webster, N.A.S.; Manuel, J.R.; Ware, N. The influence of ore composition on sinter phase mineralogy and strength. *Trans. Inst. Min. Metall. Sect. C Miner. Process. Extr. Metall.* **2016**, *125*, 140–148. [CrossRef]
18. Taira, K.; Webster, N.A.S.; Ignácio, I.R.; Ware, N.; D'Angelo, A.M.; Zhang, L.; Pownceby, M.I. Valorisation potential of low-grade fly ash as a sustainable MgO source for iron ore sintering: Insights from in-situ x-ray diffraction and tablet studies. *J. Environ. Chem. Eng.* **2024**, *12*, 112934. [CrossRef]
19. Scarlett, N.V.Y.; Pownceby, M.I.; Madsen, I.C.; Christensen, A.N. Reaction sequences in the formation of SFCA and SFCA-I in iron ore sinter. *Metall. Mater. Trans. B* **2004**, *35*, 929–936. [CrossRef]
20. Webster, N.A.S.; Pownceby, M.I.; Madsen, I.C.; Kimpton, J.A. Silico-ferrite of calcium and aluminum (SFCA) iron ore sinter bonding phases: New insights into their formation during heating and cooling. *Metall. Mater. Trans. B* **2012**, *43*, 1344–1357. [CrossRef]
21. Clout, J.M.F.; Ware, N.A.; Manuel, J.R.; Webster, N.A.S.; Pownceby, M.I. Fundamental Analysis of Sinter Solid Structure: Implications of Mineral Associations for Understanding Industrial Iron Ore Sinter Formation. *Minerals* **2026**, *16*, 129. [CrossRef]
22. Hsieh, L.-H.; Whiteman, J.A. Effect of oxygen potential on mineral formation in lime-fluxed iron ore sinter. *ISIJ Int.* **1989**, *29*, 625–634. [CrossRef]
23. Ware, N.; Manuel, J.R.; Raynlyn, T.; Lu, L. Melting behaviour of hematite and goethite fine ores and its potential impact on sinter quality. In *Proceedings of the Iron Ore Conference, Perth, WA, Australia, 12–14 August 2013*; The Australasian Institute of Mining and Metallurgy: Melbourne, Australia, 2013; pp. 485–486.
24. Ignacio, I.R.; Brooks, G.; Pownceby, M.I.; Rhamdhani, M.A.; Rankin, W.J. Effects of sintering conditions on porosity, strength, and reducibility of hematite and magnetite tablets. In Proceedings of the IMPC Asia-Pacific, Melbourne, Australia, 22–24 August 2022.
25. Honeyands, T.; Manuel, J.; Matthews, L.; Pinson, D.; Leedham, J.; Monaghan, B.; Li, H.; Chen, J.; Hayes, P.; Donskoi, E.; et al. Characterising the mineralogy of iron ore sinters—State of the art in Australia. In *Proceedings Iron Ore Conference, Perth, WA, Australia, 24–26 July 2017*; The Australasian Institute of Mining and Metallurgy: Melbourne, Australia, 2017; pp. 49–60.
26. Harrowfield, I.R.; MacRae, C.M.; Wilson, N.C. Chemical imaging in electron microprobes. *Microbeam Anal.* **1993**, *2*, 547–548.
27. Wilson, N.; MacRae, C.; Torpy, A. Analysis of combined multi-signal hyperspectral datasets using a clustering algorithm and visualisation tools. *Microsc. Microanal.* **2008**, *14*, 764–765. [CrossRef]
28. Torpy, A.; Wilson, N.C.; MacRae, C.M.; Pownceby, M.I.; Biswas, P.K.; Rahman, M.A.; Zaman, M.N. Deciphering the complex mineralogy of river sand deposits through clustering and quantification of hyperspectral x-ray maps. *Microsc. Microanal.* **2020**, *26*, 768–792. [CrossRef] [PubMed]
29. Pouchou, J.-L.; Pichoir, F. Quantitative analysis of homogeneous or stratified microvolumes applying the model "PAP". In *Electron Probe Quantitation*; Heinrich, K.F.J., Newbury, D.E., Eds.; Springer: Boston, MA, USA, 1991; pp. 31–75.
30. Webster, N.A.S.; Pownceby, M.I.; Huang, S.; Owen, N.D.; Gu, Q. In-situ x-ray diffraction analysis reveals complex calcium ferrite phase formation during heating and cooling of silico-ferrite of calcium (SFC) compositions. *ISIJ Int.* **2025**, *65*, 1588–1596. [CrossRef]
31. Webster, N.A.S.; Pownceby, M.I.; Pattel, R.; Manuel, J.R.; Kimpton, J.A. Fundamentals of silico-ferrite of calcium and aluminium (SFCA) iron ore sinter bonding phase formation: Effects of basicity and magnesium on crystallisation during cooling. *ISIJ Int.* **2019**, *59*, 263–267. [CrossRef]

Disclaimer/Publisher's Note: The statements, opinions and data contained in all publications are solely those of the individual author(s) and contributor(s) and not of MDPI and/or the editor(s). MDPI and/or the editor(s) disclaim responsibility for any injury to people or property resulting from any ideas, methods, instructions or products referred to in the content.